Biomed Environ Sci, 2022; 35(3): 215-224 215

Original Article

Direct Synthesis of Bienzyme-like Carbide-derived Carbons *via* Mild Electrochemical Oxidation of Ti_3AlC_2 MAX*

FANG Yan Feng[1,2,&], DING Xiao Teng[1,&], XU Geng Fang[1], GONG Shi Da[3], NIU Yu Sheng[1], YAO Zi Yu[4], JIN Zhao Yong[1], WANG Yao[1], and XU Yuan Hong[1,#]

1. Institute of Biomedical Engineering, College of Life Sciences, Qingdao University, Qingdao 266071, Shandong, China; 2. Jiangsu Engineering Laboratory of Smart Carbon-Rich Materials and Device, School of Chemistry and Chemical Engineering, Medical School, Southeast University, Nanjing 211189, Jiangsu, China; 3. College of Chemistry and Chemical Engineering, Qingdao 266071, Shandong, China; 4. State Key Laboratory of Silicate Materials for Architectures, Wuhan University of Technology, Wuhan 430070, Hubei, China

Abstract

Objective To develop effective alternatives to natural enzymes, it is crucial to develop nanozymes that are economical, resource efficient, and environmentally conscious. Carbon nanomaterials that have enzyme-like activities have been extensively developed as substitutes for traditional enzymes.

Methods Carbide-derived carbons (CDCs) were directly synthesized *via* a one-step electrochemical method from a MAX precursor using an ammonium bifluoride electrolyte at ambient conditions. The CDCs were characterized by systematic techniques.

Results CDCs showed bienzyme-like activities similar to that of peroxidase and superoxide dismutase. We systematically studied the dependence of CDC enzyme-like activity on different electrolytes and electrolysis times to confirm activity dependence on CDC content. Additionally, the synthesis mechanism and CDC applicability were elaborated and demonstrated, respectively.

Conclusion The demonstrated synthesis strategy eliminates tedious intercalation and delamination centrifugation steps and avoids using high concentrations of HF, high temperatures, and halogen gases. This study paves the way for designing two-dimensional material-based nanocatalysts for nanoenzyme and other applications.

Key words: Bienzyme-like; Electrochemical; Carbide-derived carbons

Biomed Environ Sci, 2022; 35(3): 215-224 *doi: 10.3967/bes2022.030* *ISSN: 0895-3988*

www.besjournal.com (full text) *CN: 11-2816/Q*

INTRODUCTION

Natural enzymes have a broad range of bioanalytical and biomedical applications[1,2]. However, intrinsic shortcomings, i.e., ease of denaturation, laborious preparation, and high cost, have limited the widespread applicability of enzymes[3]. To circumvent these issues, considerable attention has been paid to the exploration of artificial enzymes.

---

[*] This work was supported by the National Nature Science Foundation of China [No21874079]; Taishan Scholar Program of Shandong Province, Science & Technology Fund Planning Project of Shandong Colleges and Universities [J16LA13, J18KA11]; Key R&D Project of Shandong Province [GG201809230180]; and Open Funds of the State Key Laboratory of Electroanalytical Chemistry [SKLEAC202005].

[&] These authors contributed equally to this work.

[#] Correspondence should be addressed to XU Yuan Hong, Professor, Doctor, Tel: 15264285082, E-mail: yhxu@qdu.edu.cn

Biographical notes of the first authors: FANG Yan Feng, female, born in 1993, Master's Degree, majoring in synthesis and application of $Ti_3C_2T_x$ MXene-based materials; DING Xiao Teng, female, born in 1989, Assistant Professor, majoring in nano-mimetic enzymes and biosensors.

Nanomaterials that mimic enzyme properties, i.e., nanozymes, have recently garnered interest[4-7]. In the past decade, various nanozymes have been developed. Among these nanozymes, carbon-based nanozymes, including graphene, fullerenes, carbon dots, graphene quantum dots, carbon nanospheres, and carbon nanotubes, have received considerable attention due to their unique physiochemical properties, low cost, and high stability[8-10]. Carbide-derived carbons (CDCs) have attracted interest due to their large surface areas, electric properties, and high energy densities[11,12]. Atomic-level control of the carbon structure of CDCs can be derived from three-dimensional structured metal carbides. $M_{n+1}AX_n$ phases are a family of inherently ternary carbides and nitrides with hexagonal crystal structures, which are excellent precursors of two-dimensional materials synthesized through selective extraction. Here, M is an early transition metal, A is typically a group 13 or 14 element, and X represents C and/or N, with n = 1, 2, or 3. To date, CDCs, including porous carbon and carbon/sulfur nanolaminates, have been prepared through the electrochemical (EC) etching of MAX phase carbides[13,14]. However, the exfoliation of MAX phase carbides typically employs high concentration hydrogen fluoride (HF)[15], a mixture of hydrochloric acid (HCl) and lithium fluoride (LiF)[16], or high temperatures[17,18], which can be safety hazards and dangerous to the environment. The synthesis of CDCs with bienzymatic activities *via* environmentally conscious reagents and mild reaction conditions is rarely reported.

Here, CDCs were synthesized *via* a one-step EC method directly from MAX precursors using an ammonium bifluoride (NH_4HF_2) electrolyte at ambient conditions. As-synthesized CDCs showed efficient bienzymatic activities similar to that of peroxidase and superoxide dismutase (SOD). We studied the dependence of the enzyme-like activity of CDCs on different electrolytes and electrolysis times of the Ti_3AlC_2 MAX. We discussed the electrochemical exfoliation mechanism of the CDCs and tested the practicality of the CDC nanozymes *via* cholesterol detection.

EXPERIMENTAL METHODS

Materials

Bulk Ti_3AlC_2 (MAX) was obtained from Beijing Jinhezhi Materials Co., Ltd. NH_4HF_2, $NaHF_2$, NH_4F, acetic acid, sodium acetate, hydrogen peroxide (H_2O_2), sodium hydroxide (NaOH), HCl, riboflavin, methionine, nitrotetrazolium blue chloride (NBT), and 3,3',5,5'-Tetramethylbenzidine (TMB) were obtained from Sigma-Aldrich Chemical Co. (Milwaukee, WI). 3-(N-morpholino)propanesulfonic acid (MOPS) sodium salt (98%), peroxidase from horseradish (HRP), cholesterol oxidase (ChOx), cholesterol, tetracycline hydrochloride, and europium (III) chloride ($EuCl_3 \cdot 6\ H_2O$) were purchased from Shanghai Macklin Biochemical Co. Ltd., China. All reagents were analytical grade and used without further purification. Ultrapure water (18.2 MΩ/cm) was obtained from a MilliQ ultrapure system (Qingdao, China).

Characterization

UV-vis absorbance spectra were measured on a Mapada UV 6300 spectrophotometer (Shanghai, China). Generated O_2 was measured using a JPB portable oxygen-sensitive electrode (Hangzhou Qiwei Instrument Power Equipment Research Institute, China). Atom force microscopy (AFM) was carried out on a SPI3800N microscope (Seiko Instruments Inc.) operating in tapping mode. Powder X-ray diffraction (XRD) patterns were measured by a Bruker D2 PHASER diffractometer using Cu-Kα radiation (λ = 0.1542 nm). The morphology of as-prepared CDCs was characterized *via* transmission electron microscopy (TEM, JEOL JEM-2100F, Japan) with an accelerating voltage of 200 kV. Fourier transform infrared (FTIR) spectra were measured on a Nicolet 5700 FTIR spectrometer (Thermo Electron Scientific Instruments Corp., USA). X-ray photoelectron spectroscopy (XPS) was carried out using a surface analysis system with monochromatic Al-Kα (1486.6 eV) radiation (Kratos AXIS Ultra^{DLD}, Manchester, UK).

Fabrication of the CDCs

In a typical experiment, bulk MAX was applied as the anode (Supplementary Figure S1, available in www.besjournal.com) and a Pt electrode was used as the cathode. A constant 3 V DC potential was applied to the system with varying times and electrolytes (NH_4HF_2, $NaHF_2$, NH_4F) at room temperature. The suspension was collected by centrifuging at 10,000 rpm for 10 min, and the precipitate was freeze-dried without post-washing. The suspension was then dialyzed in a 1,000 Da dialysis bag for 6 h and stored at room temperature for further characterization and application.

Peroxidase Mimetic Activity of the CDCs

The enzyme kinetics of CDC samples were

monitored at 652 nm at 40 °C after 10 min incubation. Experiments were carried out using 200 μL of CDCs in 50 mmol/L NaAc buffer (pH 5.0) containing different concentrations of H_2O_2 and TMB as the substrates. The apparent kinetic parameters were obtained *via* the Michaelis-Menten equation:

$$V = \frac{V_{\max} \times [S]}{K_m + [S]}$$

where V stands for the initial velocity, V_{max} represents the maximal reaction velocity, $[S]$ is the substrate concentration, and K_m stands for the Michaelis constant. K_m and V_{max} were obtained by the Lineweaver-Burk plot method.

Superoxide Dismutase-like Catalytic Activity of CDCs

The SOD behavior of CDCs were measured *via* NBT inhibition. Mixtures containing 20 μmol/L riboflavin, 0.013 mol/L methionine, 75 μmol/L NBT, and different volumes of CDCs were prepared in 50 mmol/L NaAc buffer at pH 7.0 and 25 °C. Upon UV illumination for 10 min, reduced NBT was detected at 560 nm. For control experiments, the reaction mixture was kept in the dark before the absorbance measurement. Detailed information is presented in the Supporting Information.

SOD Assay of CDC

To confirm SOD-like catalytic activity, europium (III) chloride hexahydrate, MOPS sodium salt, tetracycline hydrochloride, and H_2O_2 were used. The weakly fluorescent Eu^{3+}-tetracycline complex (EuTc) was used as a fluorescent probe for H_2O_2 detection. Various volumes of CDC-NH_4HF_2-16h, ranging from 10 to 150 μL, were added to a 3 mL EuTc solution. A dissolved oxygen meter was used to monitor the concentration of O_2 generated during the catalytic process. Different volumes of CDC-NH_4HF_2-16h were added to a 10 mL 50 mmol/L NaAc buffer solution (pH 5).

To investigate H_2O_2 catalyzed by CDC-NH_4HF_2-16h, the following solutions were used:

A) MOPS buffer solution (10 mmol/L): MOPS sodium salt was dissolved in 800 mL of MilliQ water, and the pH was set to 6.9. A volumetric flask was filled with 1 L with MilliQ water, and the solution was homogenized.

B) $EuCl_3$ solution (6.3 mmol/L of Eu^{3+}): 115.3 mg of $EuCl_3 \cdot 6\,H_2O$ was dissolved in 50 mL of solution (A).

C) Tetracycline hydrochloride solution (2.1 mmol/L): 50.5 mg of tetracycline hydrochloride was dissolved in 50 mL of solution (A).

D) EuTc solution: 5 mL of solution (B) and (C) were mixed and with solution (A) for a final volume of 100 mL.

Cholesterol Detection using CDC as the Catalyst

10 μL ChOx (0.5 mg/mL) and 200 μL of different cholesterol concentrations were added to NaAc buffer (800 μL, 0.5 mmol/L, pH 7.0) and incubated at 37 °C for 120 min. Then, 500 μL of CDC and 200 μL of TMB (5 mmol/L) were added to the reaction mixture, followed by incubation at 40 °C for 5 min. The maximum absorbance of $TMB^{\bullet +}$ was measured at 652 nm.

DFT Calculations

Optimization calculations were performed using B97X-D/Def2-TZVP[19,20]. Molecular surface evaluation and cation size measurements were carried out *via* the Multiwfn program (version 3.6)[21] using DFT-ωB97X-D/def2-TZVP.

RESULTS

The EC exfoliation of MAX was conducted using bulk Ti_3AlC_2 MAX and a Pt electrode as the anode and cathode, at ambient conditions, respectively (Figure 1). An aqueous solution of 0.5 mol/L NH_4HF_2 was used as the electrolyte, which contained the necessary cations for interplanar intercalation as well as fluoro-containing groups for Al layer etching in the MAX exfoliation. This process avoids the utilization of concentrated HF. To confirm the role of the electrolyte in the EC exfoliation process, two other inorganic salts, i.e., ammonium fluoride (NH_4F) and sodium acid fluoride ($NaHF_2$), which possess either the same cation or anion as NH_4HF_2, respectively, were applied as electrolytes for comparison.

The influence of a constant 3V potential during the EC process at different time points (0, 1, 2, 4, 5,

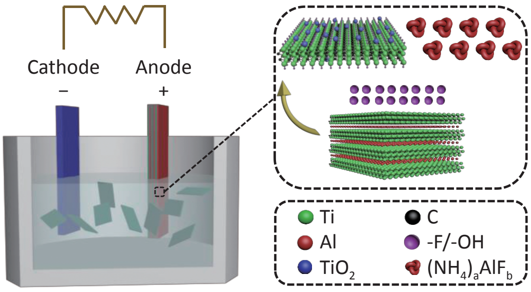

Figure 1. Schematic illustration of the exfoliation process of Ti_3AlC_2 with NH_4HF_2 as the electrolyte using the one-step EC method.

6, 8, 10, 16, 20, 22, and 24 h) on the preparation of CDCs was investigated. The color of the NH_4HF_2 electrolyte changed from colorless (Supplementary Figure S2A available in www.besjournal.com) to muddy after 1 h (Supplementary Figure S2B). The color then became yellow (Supplementary Figure S2C) after 2 h, and brown (Supplementary Figure S2D) after 4 h. Finally, the color of the mixture became dark brown (Supplementary Figure S2E) after 5 h, and then black after 6 h (Supplementary Figure S2F), indicating the exfoliation of Ti_3AlC_2 MAX to $Ti_3C_2T_x$ MXene and CDCs. The color of the suspension became more brown until 16 h, after which the color faded when the electrolysis time was extended to 20 h (Supplementary Figure S2G). Gas bubbles were observed surrounding the anode throughout the entire experiment. We note that reaction times of 6 and 16 h were the two critical time points during the electrolysis process. The obtained products from these two time points, denoted as CDCs-NH_4HF_2-6h and CDCs-NH_4HF_2-16h, respectively, were collected for further characterization. When NH_4F or $NaHF_2$ were used as electrolytes at the same concentration as NH_4HF (0.5 mol/L), the electrolyte solution also changed color over time. However, the color changes were not as obvious as that of NH_4HF_2, and only a gray color was observed for NH_4F, even after 24 h. This phenomenon demonstrated the superior efficiency of NH_4HF_2 for the exfoliation of MAX to MXene. Three obtained products at the 6 h time point, termed CDCs-NH_4HF_2-6h, CDCs-NH_4F-6h, and CDCs-$NaHF_2$-6h, were selected for further characterization.

XRD patterns of CDCs-NH_4HF_2-6h, CDCs-$NaHF_2$-6h, and CDCs-NH_4F-6h are shown in Supplementary Figure S3 (available in www.besjournal.com). The (002) reflection of $Ti_3C_2T_x$ at *ca.* 8.84° from CDCs-NH_4HF_2-6h was more obvious compared with CDCs-$NaHF_2$-6h, indicating that NH_4HF_2 had a greater MAX exfoliation than that of $NaHF_2$. However, the characteristic MXene peak was faintly detected for NH_4F, indicating that HF^- is more favorable for the EC exfoliation of MAX to MXene. XPS spectra of CDCs-NH_4HF_2-6h, CDCs-$NaHF_2$-6h, and CDCs-NH_4F-6h are shown in Supplementary Figure S4, available in www.besjournal.com. Ti 2p and O 1s peak positions of the samples are shown in Supplementary Table S1, available in www.besjournal.com. The atomic ratios of Ti from the XPS survey spectra were 8.75%, 1.59%, and 0.71% in CDCs-NH_4HF_2-6h, CDCs-$NaHF_2$-6h, and CDCs-NH_4F-6h, respectively. These results were consistent with the XRD patterns. Na^+ and NH_4^+ cations could be inserted into the interspace of $Ti_3C_2T_x$ nanosheets, thus enlarging interplanar spacing during the etching process (Supplementary Figure S5, available in www.besjournal.com). The diameters of Na^+ and NH_4^+ were the farthest spacings between all surface points. The cation surfaces were defined as isosurfaces with an electron density of ρ = 0.002 a.u.[22] Since the radius of NH_4^+ (1.8685 Å) is much larger than that of Na^+ (0.934 Å), the geometries of these two cations were calculated *via* theoretical optimization using Gaussian 16 (version B01)[23]. A more effective intercalation effect from NH_4HF_2 compared with $NaHF_2$ is expected for the $Ti_3C_2T_x$ MXene nanosheets[24]. The better etching by NH_4HF_2 and $NaHF_2$ compared with NH_4F was due to volatile H_2 production from HF_2^- at the anode during the EC process. Thus, NH_4HF_2 was confirmed to be the optimal electrolyte for the efficient exfoliation of MAX into CDCs through EC oxidative cleavage.

To further investigate the electrochemical exfoliation process, precipitates prepared in 0.5 mol/L NH_4HF_2, $NaHF_2$, and NH_4F after 6 h of EC oxidation (termed CDCsP-NH_4HF_2-6h, CDCsP-$NaHF_2$-6h, and CDCsP-NH_4F-6h, respectively) were collected for XRD characterization after centrifugation and freeze-drying without post-washing. As shown in Figure 2, the XRD patterns of CDCs-NH_4HF_2-6h and CDCs-NH_4F-6h showed three main byproducts, i.e., $(NH_4)_3AlF_6$, NH_4AlF_4, and $AlF_3{\cdot}3H_2O$. Additionally, Na_3AlF_6, $NaAlF_4$, and $AlF_3{\cdot}3H_2O$ were the main byproducts of CDCs-$NaHF_2$-6h. The XRD patterns of CDCs-NH_4HF_2-6h and CDCs-$NaHF_2$-6h (Supplementary Figure S3) showed a (002) peak of $Ti_3C_2T_x$ in the electrolyte, with the exfoliation mechanism of this process as:

$$NH_4/NaHF_2 \rightarrow NH^+{}_4/Na + HF^-{}_2$$

$$HF^-{}_2 \rightarrow HF + F^-$$

$$Ti_3AlC_2 + HF + NH^+{}_4/Na \rightarrow (NH_4)_a/NaAlF_b + AlF_3 + H_2\uparrow + Ti_3C_2$$

$$AlF_3 + cH_2O \rightarrow AlF_3{\cdot}cH_2O$$

$$Ti_3C_2 + NH_4/NaHF_2 + H_2O \rightarrow Ti_3C_2Fx(OH)_yX_z\,(MXene)$$

$$Ti_3C_2F_x(OH)_y(NH_4)_z \xrightarrow{EC} C$$

where a, b, c, x, y, and z represent different numbers, while $Ti_3C_2F_x(OH)_yX_z$ is the accurate chemical formula of $Ti_3C_2T_x$.

Metallic M–A bonds are relatively weak compared with M–X bonds; thus, “A” layers in MAX phases are removed. Based on these results, we conclude that the EC etching of Ti_3AlC_2 MAX into $Ti_3C_2T_x$ and CDCs occurs in two steps. First, HF_2^- is ionized to HF and F^-. The HF attacks the Al layer, which is successfully etched, and –F functional groups as well as –OH and –O are formed on the Ti_3C_2 MXene due to the dissolved oxygen in the aqueous medium. Second, the outside layer of the MXene ($Ti_3C_2F_x(OH)_yX_z$) is further etched, resulting in the formation of amorphous carbon with –Cl, –OH, and –O terminal groups *via* the simultaneous removal of both M and A atoms. More efficient etching agents and longer electrolysis times should result in higher CDC concentrations. TEM and HRTEM characterization was carried out to confirm the morphology and crystallinity of CDCs-NH_4HF_2-6h and CDCs-NH_4HF_2-16h.

Many small CDCs were uniformly observed for the two samples (Figure 3A and 3B). The average diameter of CDCs-NH_4HF_2-6h and CDCs-NH_4HF_2-16h was calculated to be 230 ± 30 and 37 ± 5 nm, from counting 100 particles, respectively (Figure 3A and 3B insets). Additionally, an average in-plane lattice spacing of 0.34 nm was observed for the crystalline structure of CDCs-NH_4HF_2-6h, which indicated the (002) facet as carbon (Figure 3C). An interplanar space of 0.23 nm was also observed, which resulted from the (103) crystal face of the $Ti_3C_2T_x$ MXene (Figure 3C)[25]. Less lattice fringe, corresponding to a lower crystallinity, was obtained for CDCs-NH_4HF_2-16h, indicative of the generation of amorphous CDCs (Figure 3D) upon extended electrochemical oxidation. The HRTEM results were consistent with the XRD data. There was also a broad peak around $2θ$ = 20 to 30° in the XRD pattern of CDCs-NH_4HF_2-6h, suggesting the appearance of a (002) facet of carbon with a low degree of graphitization (Supplementary Figure S3, red line)[26]. This graphitic peak from CDCs-NH_4HF_2-16h was much weaker and broader than that of CDCs-NH_4HF_2-6h, suggesting that CDCs-NH_4HF_2-16h was more disordered due to the further electrochemical oxidation of carbon[27] (Figure 3E). Elemental mapping characterization showed that C, F, and O were homogenously dispersed (Figure 3F). AFM measurements (Figure 3G) and corresponding height analyses (Figure 3H) revealed that nanosheets were well dispersed in the aqueous suspension, with topographic heights ranging from 2.7 to 4.5 nm, and that the majority of CDCs-NH_4HF_2-16h were 3-5-layer structures. FTIR spectra indicated that both CDCs-NH_4HF_2-6h and CDCs-NH_4HF_2-16h exhibited identical stretching vibrations, including –OH at 3,430 cm^{-1}, C=O at 1,630 cm^{-1}, O–H at around 1,380 cm^{-1}, C–F at around 1,050 cm^{-1}, and Ti-O at around 713 cm^{-1}[28] (Figure 3I).

To further confirm the effects of electrolysis time, samples at two other reaction time points, i.e., CDCs-NH_4HF_2-10h and CDCs-NH_4HF_2-20h, were characterized *via* XPS. C, Ti, O, and F were observed in the survey spectra for all four samples (Supplementary Figure S6A, C, E, and G, available in www.besjournal.com). C 1s, Ti 2p, and O 1s peak positions of the samples are shown in Table S2. Peaks at 281.75 (282) eV, 284.4 (284.55, 284.41, or 284.3) eV, and 284.85 (285, 285, or 284.99) eV correspond to Ti–C, C–C, and C–O, respectively (Supplementary Figure S6B, D, F, and H). The intensity of the Ti–C peak gradually decreased, demonstrating that MAX was transformed into MXene, and then oxidized to C. For the Ti 2p region, peaks at 466 (466, 465.79, or 465.8) eV and 460.25 (460.3, 460.15, or 460.03) eV were attributed to Ti–O, peaks at 464.9 (465) eV and 459.15 (459.4) eV were attributed to C-Ti-Fx, and the peak at 462.9 eV corresponds to Ti^{3+}[25] (Supplementary Figure S7A, C, E, and G, available in www.besjournal.com). The intensity of the C-Ti-Fx and Ti^{3+} peaks gradually decreased when the electrolysis time was extended to 16 h, consistent with the O 1s spectra. Detailed information about the O-containing groups, including Ti-O (530.03, 530.9, 530.5, or 531 eV), C-Ti-O_x (531 or 531.6 eV), C-Ti-$(OH)_x$ (531.78 or 532.1 eV), and H_2O (532.6, 532.8, 532.13, or 532.1 eV) were derived from the O 1s spectra. The bond length of C-Ti-$(OH)_x$ decreased, further proving the conversion of

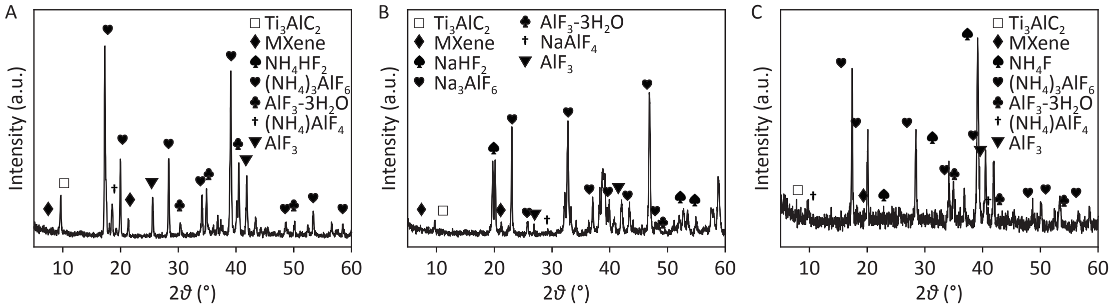

Figure 2. XRD patterns of (A) CDCs-NH_4HF_2-6h, (B) CDCs-$NaHF_2$-6h, and (C) CDCs-NH_4F-6h.

$Ti_3C_2T_x$ MXene (Supplementary Figure S7B, D, F, and H). The atomic ratios of C from XPS survey spectra were 32.6%, 41.96%, 63.08%, and 32.48% from CDCs-NH_4HF_2-6h, CDCs-NH_4HF_2-10h, CDCs-NH_4HF_2-16h, and CDCs-NH_4HF_2-20h, respectively. The carbon content reached a maximum value at an electrolysis time of 16 h, indicating that $Ti_3C_2T_x$ was consumed and transformed to carbon. The carbon content in CDCs-NH_4HF_2-20h decreased with ongoing time, which was attributed to further carbon oxidation in the presence of dissolved oxygen from the aqueous medium[29]. These results are consistent with the color of CDCs fading after 16 h (Supplementary Figure S2G). Based on these results, CDCs-NH_4HF_2-16h was determined as the optimal CDC for this carbon-nanozyme study.

DISCUSSION

A schematic illustration of CDCs-NH_4HF_2-16h-catalyzed oxidation of TMB by H_2O_2 is shown in Figure 4A. The intrinsic peroxidase mimetic activity of CDCs-NH_4HF_2-16h was studied using TMB as a chromogenic substrate for H_2O_2. In the absence of CDCs-NH_4HF_2-16h, the solution of TMB and H_2O_2 was colorless. This phenomenon was also observed for

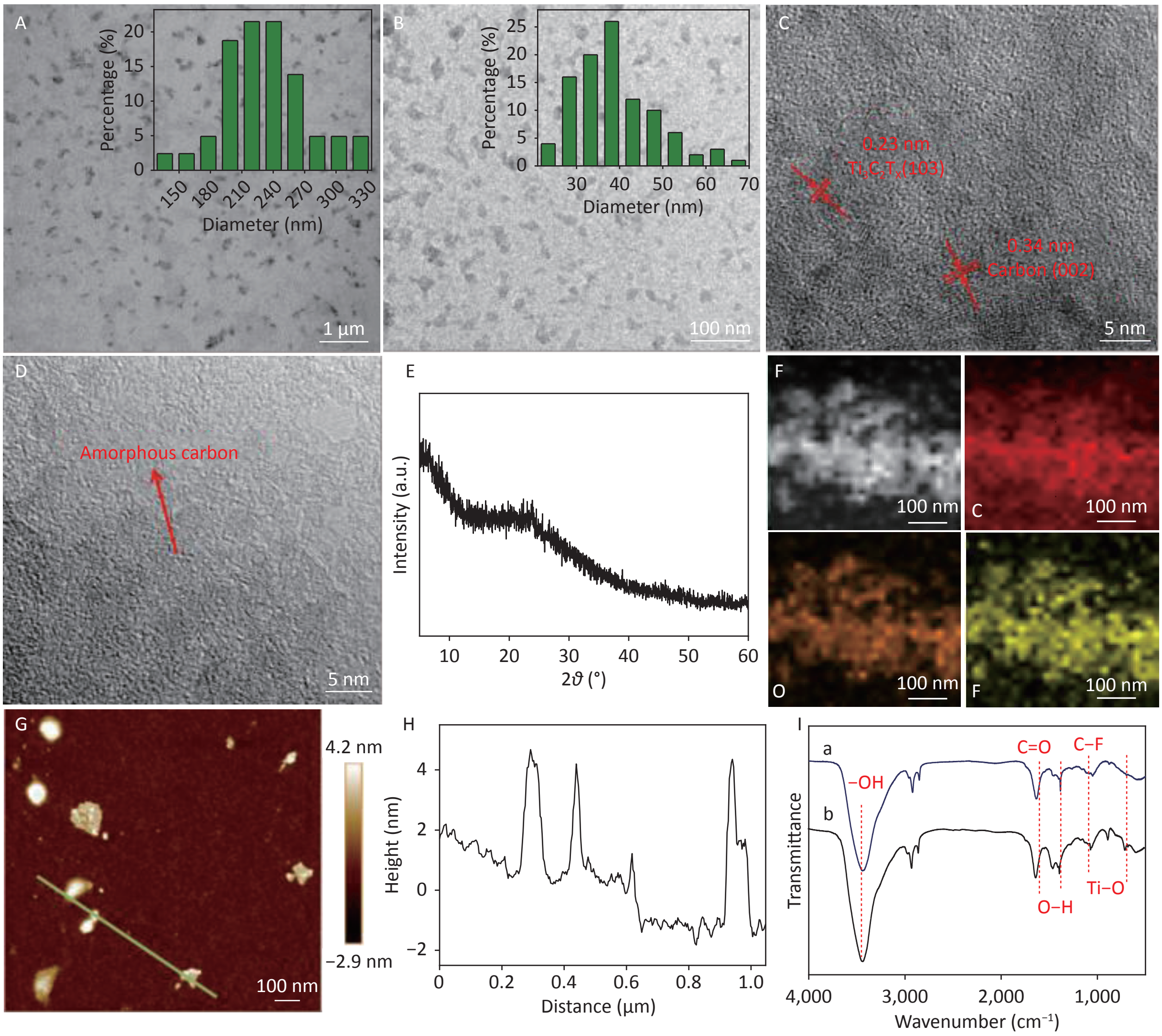

Figure 3. (A, B) TEM and (C, D) HRTEM images of (A, C) CDCs-NH_4HF_2-6h and (B, D) CDCs-NH_4HF_2-16h. (E) XRD pattern of CDCs-NH_4HF_2-16h; (F) TEM and corresponding elemental mapping images of C, O, and F in CDCs-NH_4HF_2-16h. (G) AFM topography of CDCs-NH_4HF_2-16h. (H) Height profiles from the white line section in the AFM image. (I) FTIR spectra of CDCs-NH_4HF_2-6h and CDCs-NH_4HF_2-16h. Insets (A, B) are particle size distributions obtained from TEM.

either TMB or H_2O_2 alone with CDCs-NH_4HF_2-16h. However, in the presence of CDCs-NH_4HF_2-16h, TMB reacts with H_2O_2 to generate TMB$^{\bullet+}$, which showed a characteristic absorption peak at 652 nm (Supplementary Figure S8, available in www.besjournal.com). An obvious TMB$^{\bullet+}$ absorbance peak was observed for the system containing CDCs-NH_4HF_2-16h, H_2O_2, and TMB (Figure 4B). Photographs of the different systems are shown in the inset of Figure 4B, which confirmed the intrinsic peroxidase-like activity of CDCs-NH_4HF_2-16h. The pH and temperature tolerance of the peroxidase-like behavior of CDCs-NH_4HF_2-16h and HRP were compared at various temperatures (5–95 °C) and different pHs (1–12). The optimal pH of CDCs-NH_4HF_2-16h was 5.0, which was similar to the value (pH 4.0) for HRP (Figure 4C). As shown in Figure 4D, the optimal temperature for HRP was 35 °C. The catalytic performance decayed at either increasing or decreasing temperatures. In contrast, the catalytic activity of CDCs-NH_4HF_2-16h increased with increasing temperature (even up to 95 °C), indicating its thermal stability.

To study the SOD-like activity of CDCs, e.g., CDCs-NH_4HF_2-16h, the decrease of superoxide anion radicals ($O_2^{\bullet-}$) and the increase of H_2O_2 and O_2 were measured. SOD strongly enhances the disproportionation of $O_2^{\bullet-}$ into H_2O_2 and O_2 and thus inhibits the reduction of NBT *via* the mediation of $O_2^{\bullet-}$ (Figure 5A). As shown in Figure 5B, no fluorescence signal was obtained without UV irradiation in the presence of riboflavin, methionine, and NBT (curve a). Upon UV irradiation, the fluorescence signal sharply increased, indicating a high level of $O_2^{\bullet-}$ (curve b)[4]. After addition of CDCs-NH_4HF_2-16h, the fluorescence signal decreased dramatically, which confirmed that CDCs-NH_4HF_2-16h possessed SOD-like activity and could remove $O_2^{\bullet-}$ (curve c). As seen in Figure 5C, the fluorescence of the reaction system decreased with increasing

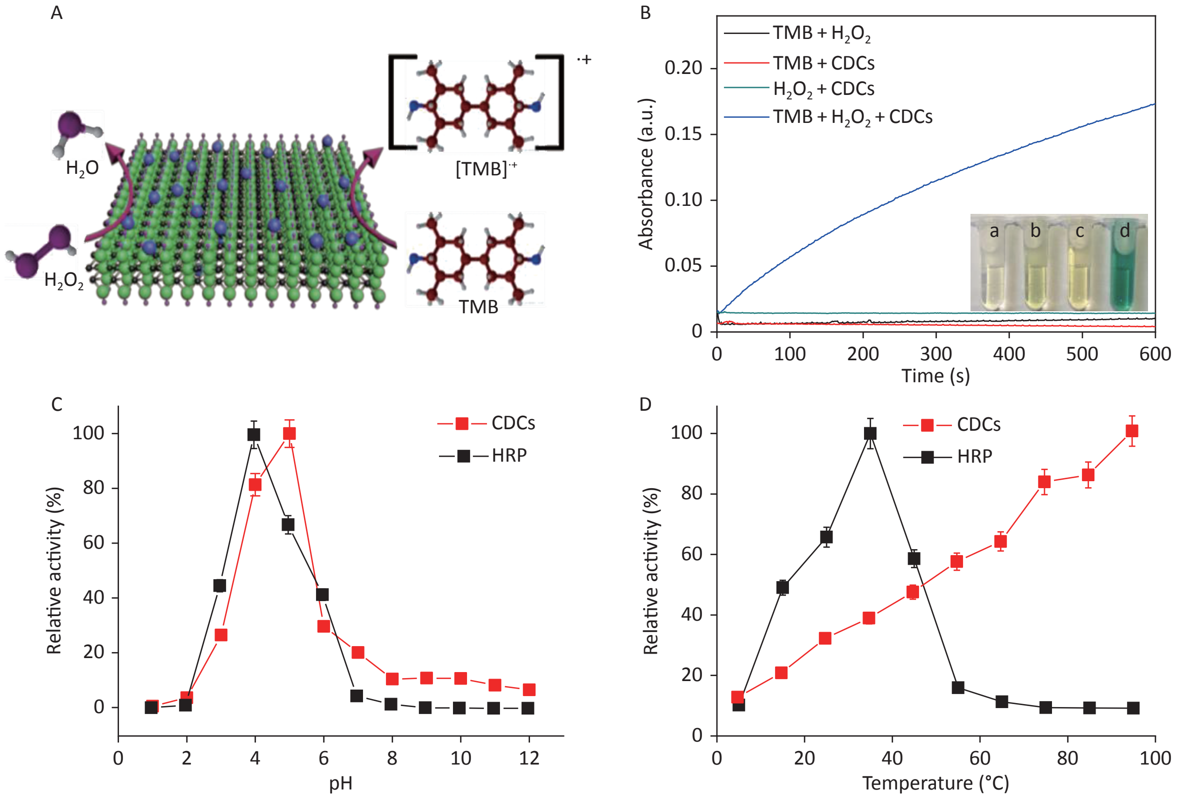

Figure 4. (A) Schematic illustration of CDCs-NH_4HF_2-16h catalyzing the oxidation of TMB in the presence of H_2O_2. (B) Time-dependent absorbance changes at 652 nm of TMB in different reaction systems in 50 mM NaAc (pH = 5) at room temperature. The inset in (B) shows the corresponding photographs: (a) a mixture of TMB and H_2O_2 in the absence of CDCs, (b) a mixture of TMB and CDCs in the absence of H_2O_2, (c) a mixture of CDCs and H_2O_2 in the absence of TMB, and (d) a mixture of TMB, H_2O_2, and CDCs. The (C) pH dependence and (D) temperature dependence of the peroxidase-like activity of nanosheets and HRP in 50 mmol/L NaAc. The H_2O_2 and TMB concentration were 50 mmol/L and 1 mg/mL, respectively.

CDCs-NH_4HF_2-16h concentration, which indicated that the scavenging efficiency of $O_2^{\bullet-}$ was directly proportional to the amount of CDCs-NH_4HF_2-16h.

The Eu^{3+}-tetracycline complex (EuTc) is not fluorescent; however, binding with H_2O_2 forms a fluorescent europium tetracycline hydrogen peroxide complex (EuTc-HP), which results in a strong enhancement in fluorescence intensity[30]. The fluorescence intensity change of EuTc at 620 nm (with λ_{ex} = 405 nm) was monitored against H_2O_2 concentration. The fluorescence signal increased with increasing amounts of H_2O_2 (Supplementary Figure S9A available in www.besjournal.com).

The fluorescence intensity of the EuTc system increased with increasing CDCs-NH_4HF_2-16h and reaction time, which confirmed the activity of CDCs-NH_4HF_2-16h as a SOD mimic for generating H_2O_2 (Supplementary Figure S9B–D). Furthermore, an oxygen-sensitive electrode was used to track the concentration of O_2 generated during the reaction. Increasing the amount of CDCs-NH_4HF_2-16h resulted in an increased formation of O_2 (Supplementary Figure S9E). These results indicated the formation of H_2O_2 and O_2 in the presence of CDCs-NH_4HF_2-16h, which demonstrated the SOD-mimic activity of the CDCs. To study the kinetics of the peroxidase-mimic activity of the CDCs, the steady-state kinetics of observed color variations were analyzed by changing TMB and H_2O_2 concentrations (Supplementary Figure S10 available in www.besjournal.com). Maximum initial reaction rates (V_{max}) were calculated from the double reciprocal of the Michaelis-Menten equation defined in the experimental section (Supplementary Table S3, Supplementary Figure S11 available in www.besjournal.com). The V_{max} of CDCs was enhanced with increasing electrolysis times, from 6 to 16 h (Supplementary Table S3). However, the V_{max}

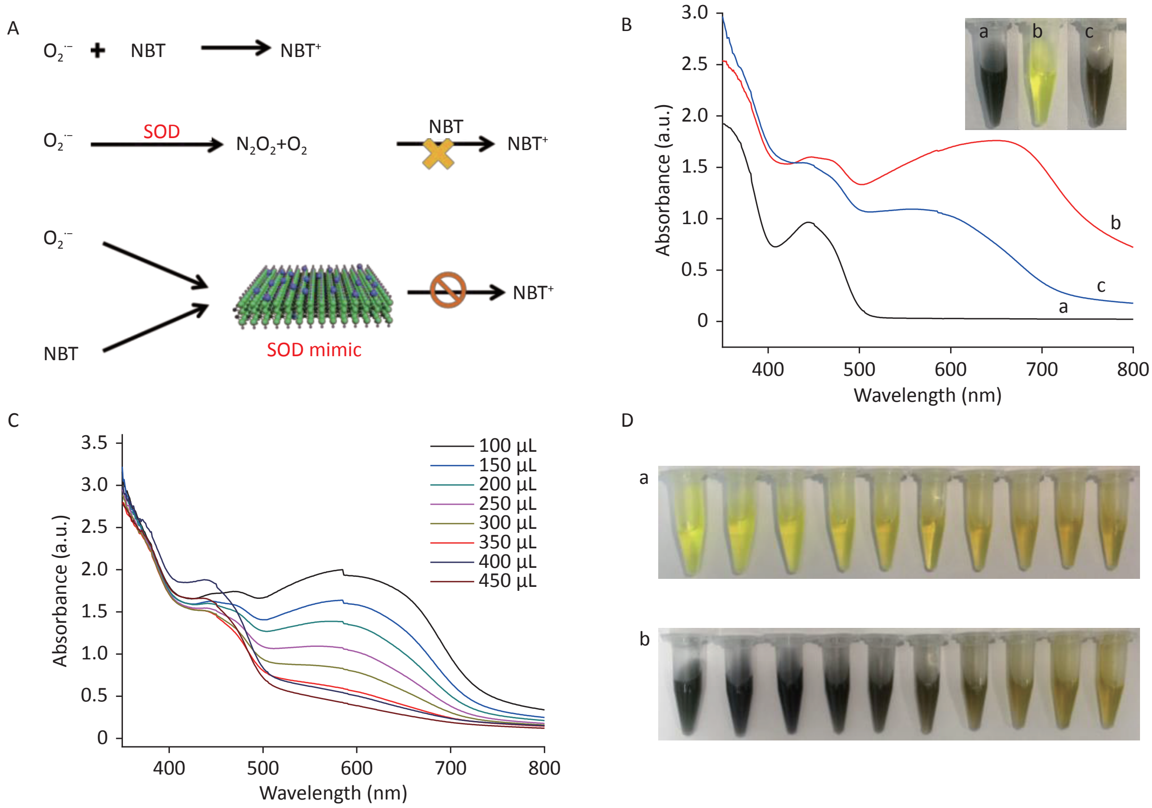

Figure 5. (A) Schematic illustration of the SOD-like activity of CDCs-NH_4HF_2-16h. (B) Scavenging efficiency of superoxide radicals in different conditions: (a) blank control without ultraviolet radiation, (b) absence, and (c) presence of CDCs-NH_4HF_2-16h after ultraviolet radiation. Inset shows corresponding photographs. (C) Scavenging efficiency of superoxide radicals with different concentrations of CDCs-NH_4HF_2-16h. (D) Photographs of the scavenging efficiency of superoxide radicals (a) before and (b) after ultraviolet radiation. The photographs show different volumes of CDCs ranging from 0 to 450 μL (50 μL increments), from left to right.

decreased with extended reaction times. The UV-vis absorption spectra of different electrolysis times, ranging from 6–24 h, confirmed that CDCs-NH_4HF_2-16h exhibited the highest enzymatic activity (Supplementary Figure S12 available in www.besjournal.com). Supplementary Figure S13 (available in www.besjournal.com) shows corresponding photographs of CDCs with different electrolysis times, ranging from 6–24 h, after the addition of TMB and H_2O_2 for 30 min. The peroxidase-like activity increased with increasing CDC content. These results confirmed that the peroxidase-like catalytic activity of CDCs was a result of the carbon material.

Due to the intrinsic peroxidase-like catalytic activity of CDCs, cholesterol detection was carried out by combining the mimetic enzyme with cholesterol oxidase. As shown in Figure 6A, the absorbance intensity at 652 nm was proportional to the cholesterol concentration, ranging from 7.79 µmol/L to 116.96 µmol/L. A linear regression equation of $I = 0.45 \times C_{\text{cholesterol}} + 0.01$ (unit of C is µmol/L) with $R^2 = 0.9928$ is shown in Figure 6B. The detection limit was determined to be 3 µmol/L ($S\ N^{-1} \geq 3$, Supplementary Figure S14 available in www.besjournal.com), which is superior or comparable to other reported nanozyme based cholesterol detection methods. These results demonstrate the broad applicability of these CDCs in both chemical and biochemical applications.

CONCLUSION

In summary, CDCs were synthesized by the one-step electrochemical exfoliation of bulk Ti_3AlC_2 in NH_4HF_2. The CDCs possessed both peroxidase- and SOD-like activity, which increased with increasing carbon content. Thus, we confirmed that the enzymatic activity resulted from the CDC material. The optimal reaction time for the peroxidase-like catalytic activity of CDCs was determined to be 16 h of the EC process. Additionally, the synthetic mechanism of CDCs was demonstrated, and possible reaction equations between Ti_3AlC_2 and bifluoride were proposed. Moreover, the applicability of the nanozymes was demonstrated by the sensitive detection of cholesterol. This synthesis strategy eliminates tedious centrifugation intercalation and delamination steps and is environmentally conscious due to the avoidance of high concentration HF, high temperatures, and halogen gases. This study paves the way for designing two-dimensional material-based nanocatalysts for nanoenzyme and other applications.

ACKNOWLEDGMENTS

We appreciate Dr. Tingting Zhang and Hao Wan for her help in some experiments, who works in the Biology Experimental Teaching Center of Qingdao University.

CONFLICTS OF INTEREST

The authors declare no conflict of interest.

Received: April 22, 2021;
Accepted: October 19, 2021

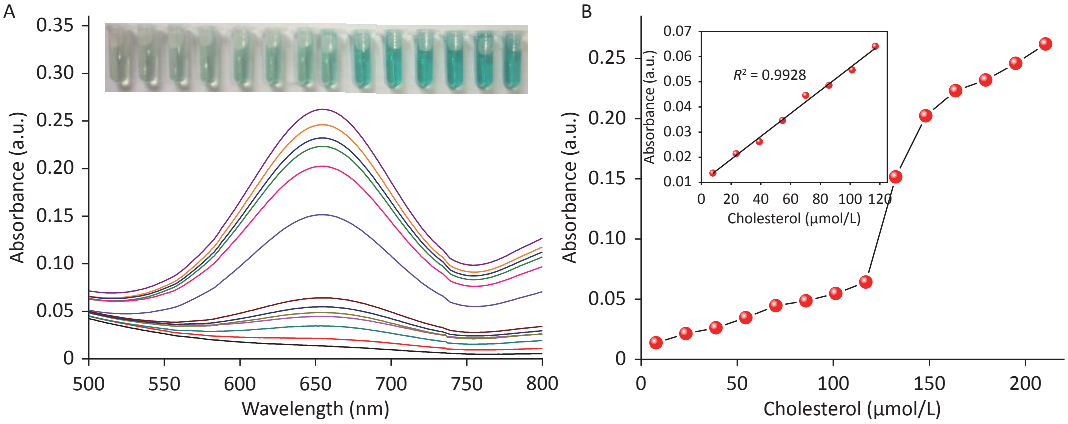

Figure 6. (A) UV-vis spectra of CDCs-NH_4HF_2-16h+TMB+ChOx with different concentrations of cholesterol (Inset: images of colored products for different concentrations of cholesterol). (B) Calibration curve of cholesterol detection (Inset: linear calibration plot of cholesterol detection).

REFERENCES

1. Mishra RK, Goud KY, Li ZH, et al. Continuous opioid monitoring along with nerve agents on a wearable microneedle sensor array. J Am Chem Soc, 2020; 142, 5991−5.
2. Huffman MA, Fryszkowska A, Alvizo O, et al. Design of an in vitro biocatalytic cascade for the manufacture of islatravir. Science, 2019; 366, 1255−9.
3. Jiang DW, Ni DL, Rosenkrans ZT, et al. Nanozyme: new horizons for responsive biomedical applications. Chem Soc Rev, 2019; 48, 3683−704.
4. Huang L, Niu YS, Li RG, et al. VO_x quantum dots with multienzyme-mimic activities and the application in constructing a three-dimensional (3D) coordinate system for accurate discrimination of the hydrogen peroxide over a broad concentration range. Anal Chem, 2019; 91, 5753−61.
5. Wu JJX, Wang XY, Wang Q, et al. Nanomaterials with enzyme-like characteristics (nanozymes): next-generation artificial enzymes (II). Chem Soc Rev, 2019; 48, 1004−76.
6. Zhang P, Sun DR, Cho A, et al. Modified carbon nitride nanozyme as bifunctional glucose oxidase-peroxidase for metal-free bioinspired cascade photocatalysis. Nat Commun, 2019; 10, 940.
7. Liang MM, Yan XY. Nanozymes: From new concepts, mechanisms, and standards to applications. Accounts Chem Res, 2019; 52, 2190−200.
8. Sun HJ, Zhou Y, Ren JS, et al. Carbon nanozymes: Enzymatic properties, catalytic mechanism, and applications. Angew Chem Int Ed, 2018; 57, 9224−37.
9. Sun HJ, Zhao AD, Gao N, et al. Deciphering a nanocarbon-based artificial peroxidase: Chemical identification of the catalytically active and substrate-binding sites on graphene quantum dots. Angew Chem Int Ed, 2015; 54, 7176−80.
10. Ding H, Hu B, Zhang B, et al. Carbon-based nanozymes for biomedical applications. Nano Res, 2021; 14, 570−83.
11. Ariyanto T, Zhang GR, Riyahi F, et al. Controlled synthesis of core-shell carbide-derived carbons through in situ generated chlorine. Carbon, 2017; 115, 422−9.
12. Wu J, Zhang XX, Li Z, et al. Toward high-performance capacitive potassium-ion storage: A superior anode material from silicon carbide-derived carbon with a well-developed pore structure. Adv Funct Mater, 2020; 30, 2004348.
13. Lukatskaya MR, Halim J, Dyatkin B, et al. Room-temperature carbide-derived carbon synthesis by electrochemical etching of MAX phases. Angew Chem Int Ed, 2014; 53, 4877−80.
14. Zhao M, Sedran M, Ling Z, et al. Synthesis of carbon/sulfur nanolaminates by electrochemical extraction of titanium from Ti_2SC. Angew Chem Int Ed, 2015; 54, 4810−4.
15. Fang YF, Yang XC, Chen T, et al. Two-dimensional titanium carbide (MXene)-based solid-state electrochemiluminescent sensor for label-free single-nucleotide mismatch discrimination in human urine. Sensor Actuat B Chem, 2018; 263, 400−7.
16. Huang HS, Jiang X, Li NJ, et al. Noble-metal-free ultrathin MXene coupled with In_2S_3 nanoflakes for ultrafast photocatalytic reduction of hexavalent chromium. Appl Catal B:Environ, 2021; 284, 119754.
17. Li YB, Li M, Lu J, et al. Single-atom-thick active layers realized in nanolaminated $Ti_3(Al_xCu_{1-x})C_2$ and its artificial enzyme behavior. ACS Nano, 2019; 13, 9198−205.
18. Fashandi H, Dahlqvist M, Lu J, et al. Synthesis of Ti_3AuC_2, $Ti_3Au_2C_2$ and Ti_3IrC_2 by noble metal substitution reaction in Ti_3SiC_2 for high-temperature-stable Ohmic contacts to SiC. Nat Mater, 2017; 16, 814−8.
19. Chai JD, Head-Gordon M. Long-range corrected hybrid density functionals with damped atom-atom dispersion corrections. Phys Chem Chem Phys, 2008; 10, 6615−20.
20. Weigend F, Ahlrichs R. Balanced basis sets of split valence, triple zeta valence and quadruple zeta valence quality for H to Rn: Design and assessment of accuracy. Phys Chem Chem Phys, 2005; 7, 3297−305.
21. Lu T, Chen FW. Multiwfn: A multifunctional wavefunction analyzer. J Comput Chem, 2012; 33, 580−92.
22. Bader RFW, Henneker WH, Cade PE. Molecular charge distributions and chemical binding. J Chern Phys, 1967; 47, 3341−63.
23. Frisch MJ, Trucks GW, Schlegel HB, et al. Gaussian 16 (Revision B. 01). Wallingford, CT: Gaussian, Inc. , 2016.
24. Feng AH, Yu Y, Wang Y, et al. Two-dimensional MXene Ti_3C_2 produced by exfoliation of Ti_3AlC_2. Mater Des, 2017; 114, 161−6.
25. Fang YF, Liu ZC, Han JR, et al. High-performance electrocatalytic conversion of N_2 to NH_3 using oxygen-vacancy-rich TiO_2 in situ grown on $Ti_3C_2T_x$ MXene. Adv Energy Mater, 2019; 9, 1803406.
26. Zhao Z, Yuan ZK, Fang ZS, et al. In situ activating strategy to significantly boost oxygen electrocatalysis of commercial carbon cloth for flexible and rechargeable Zn-Air batteries. Adv Sci, 2018; 5, 1800760.
27. Pan L, Wang YX, Hu H, et al. 3D self-assembly synthesis of hierarchical porous carbon from petroleum asphalt for supercapacitors. Carbon, 2018; 134, 345−53.
28. Xue Q, Zhang HJ, Zhu MS, et al. Photoluminescent Ti_3C_2 MXene quantum dots for multicolor cellular imaging. Adv Mater, 2017; 29, 1604847.
29. Ghassemi H, Harlow W, Mashtalir O, et al. *In situ* environmental transmission electron microscopy study of oxidation of two-dimensional Ti_3C_2 and formation of carbon-supported TiO_2. J Mater Chem A, 2014; 2, 14339−43.
30. Hu MH, Korschelt K, Daniel P, et al. Fibrous nanozyme dressings with catalase-like activity for H_2O_2 reduction to promote wound healing. ACS Appl Mater Interfaces, 2017; 9, 38024−31.

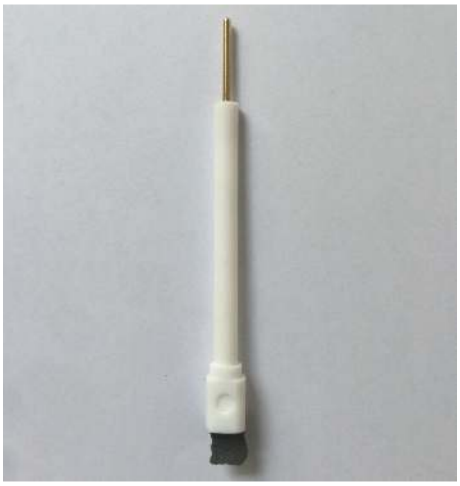

Supplementary Figure S1. The installation of positive electrode.

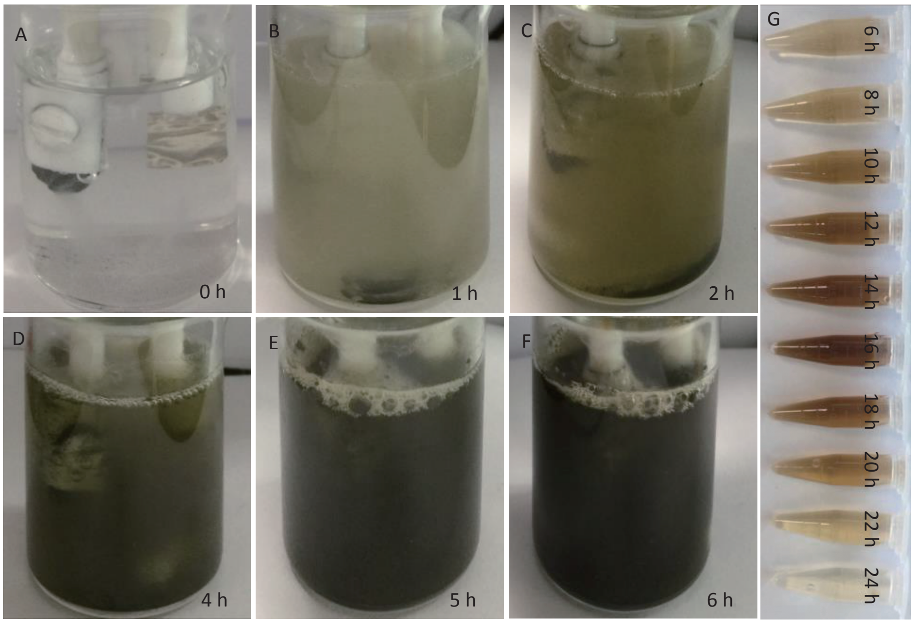

Supplementary Figure S2. Photographs of the reaction mixtures from the EC generation process at different time periods: (A) 0 h, (B) 1 h, (C) 2 h, (D) 4 h, (E) 5 h, and (F) 6 h, respectively; (G) The photographs of the supernatant upon different electrolytic time.

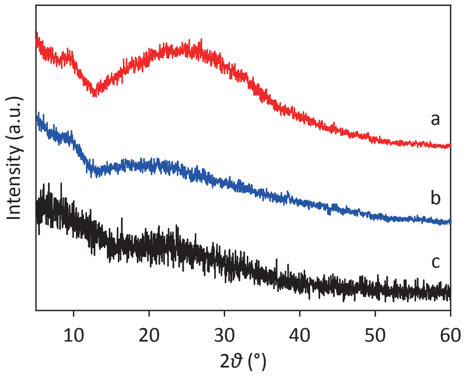

Supplementary Figure S3. XRD patterns of (a) CDCs-NH_4HF2-6h, (b) CDCs-NaHF2-6h, (c) CDCs-NH_4F-6h, respectively.

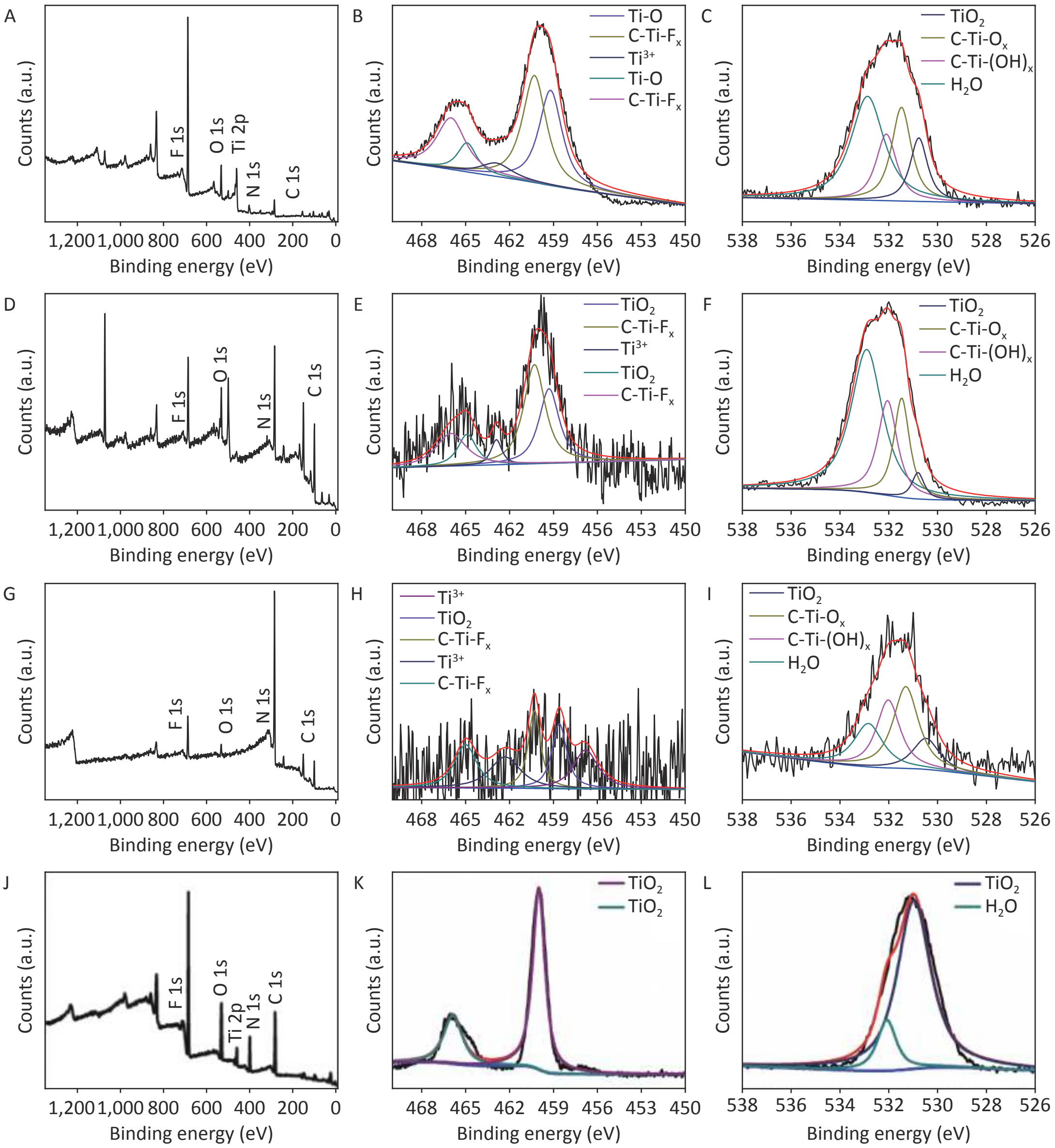

Supplementary Figure S4. The survey XPS spectra (A, D, and G), the narrow scan spectra of Ti 2p (B, E, and H) and O 1s (C, F, and I) of the CDCs-NH_4HF2-6h, CDCs-NaHF2-6h, and CDCs-NH_4F-6h, respectively.

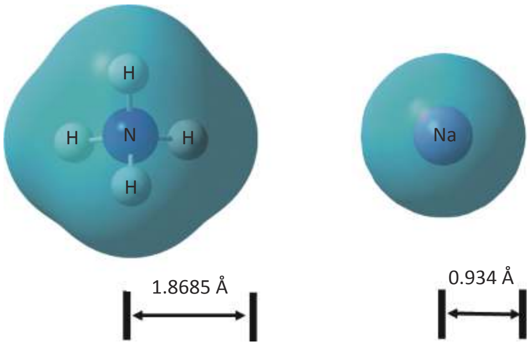

Supplementary Figure S5. The cation radius of NH^{+}_{4} and Na^{+}.

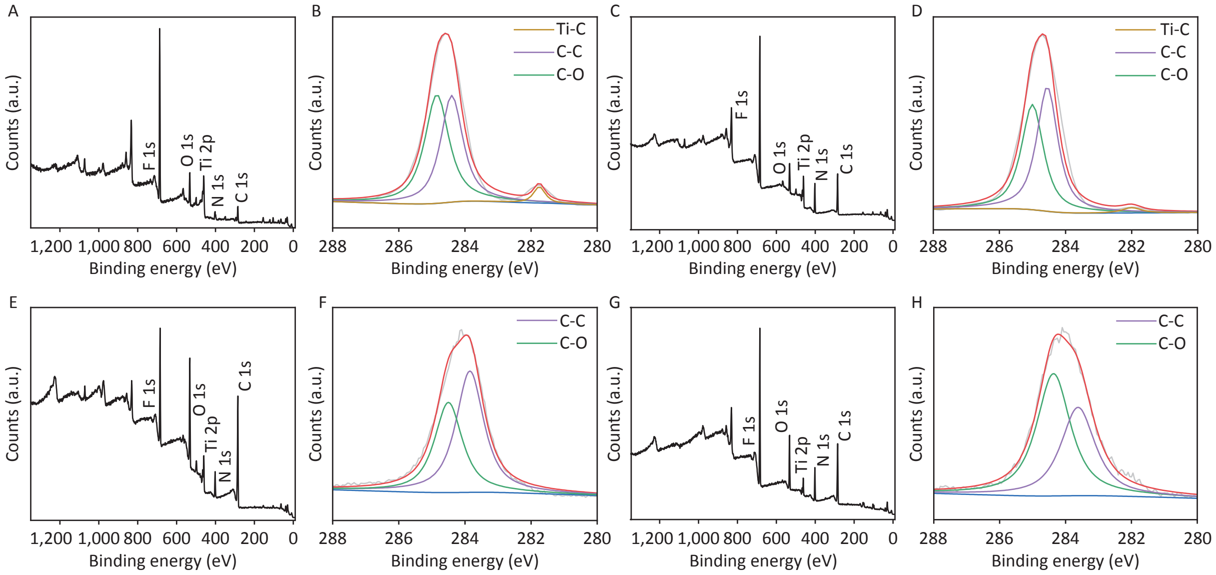

Supplementary Figure S6. The survey XPS spectra (A, C, E, and G) and the narrow scan spectra of C 1 s (B, D, E, and H) of the CDCs-NH_4HF2-6h, CDCs-NH_4HF2-10h, CDCs-NH_4HF2-16h, and CDCs-NH4HF2-20h, respectively.

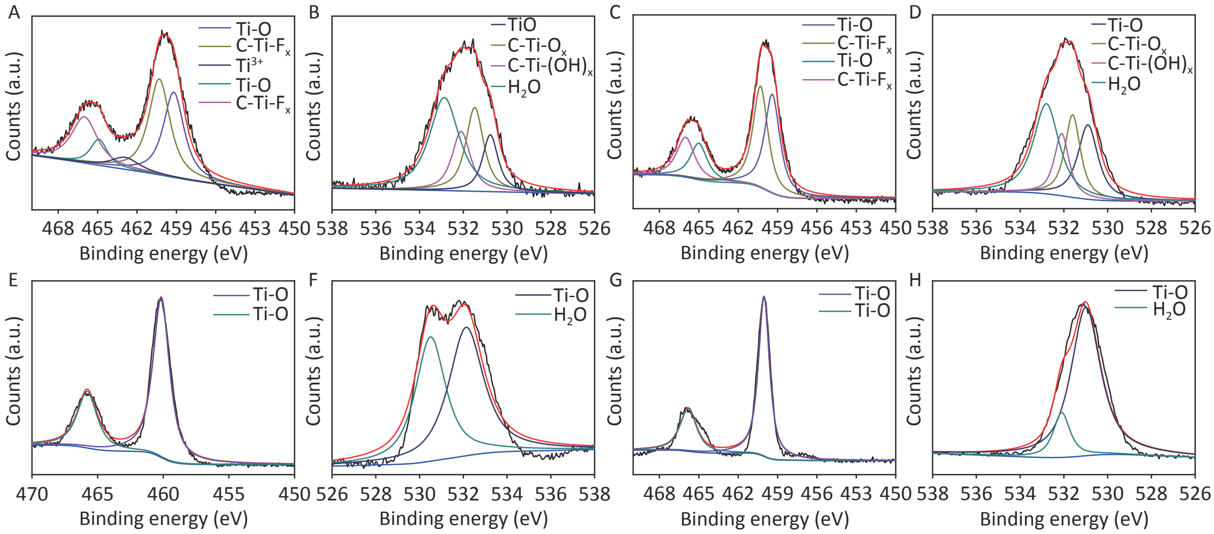

Supplementary Figure S7. The survey XPS spectra of Ti 2p (A, C, E, and G) and O 1s (B, D, F, and H) of the CDCs-NH_4HF_2-6h, CDCs-NH_4HF_2-10h, CDCs-NH_4HF_2-16h, and CDCs-NH_4HF_2-20h, respectively.

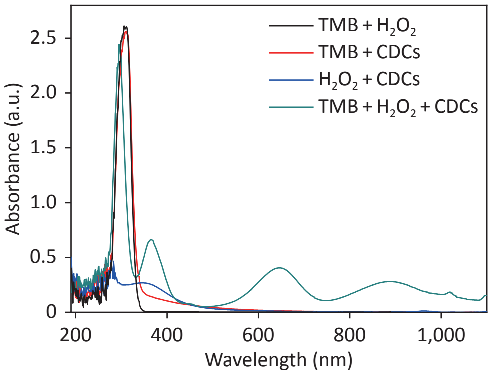

Supplementary Figure S8. UV-vis adsorption spectra of different reaction systems in a 50 mmol/L NaAc (pH = 5) at room temperature. (a) Photography of the mixture of TMB and H_2O_2 in the absence of CDCs. (b) Photography of the mixture of TMB and CDCs in the absence of H_2O_2. (c) Photography of the mixture of CDCs and H_2O_2 in the absence of TMB. (d) Photography of the mixture of TMB, H_2O_2 and CDCs. The H_2O_2 and TMB concentration were 50 mmol/L, 1 mg/mL, respectively.

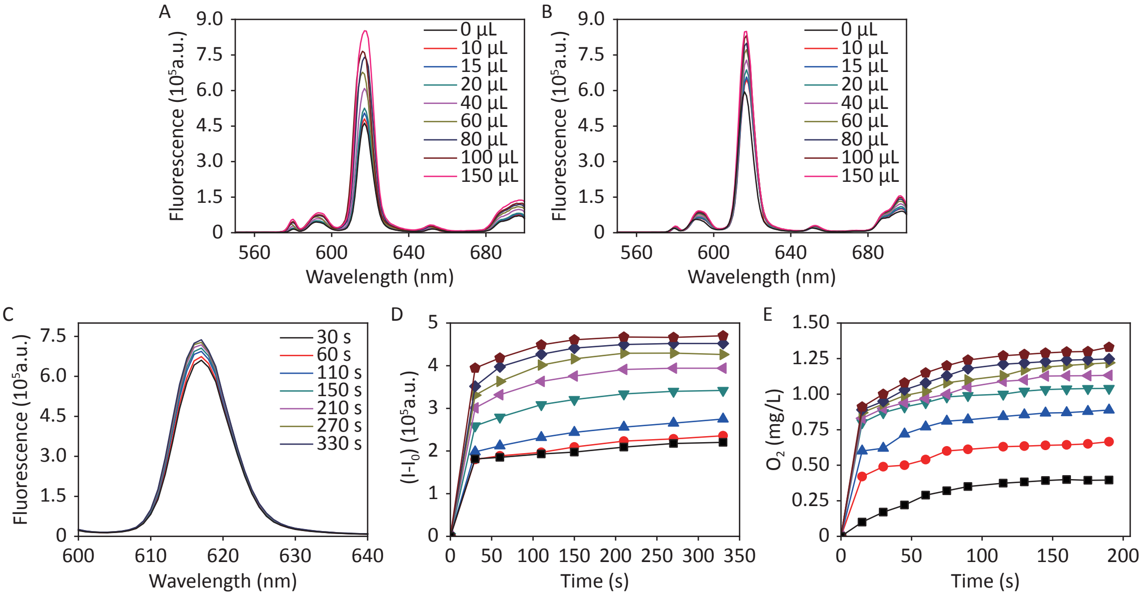

Supplementary Figure S9. The fluorescence spectra of EuTc solutions in the presence of different volumes of (A) H_2O_2 and (B) CDCs-NH_4HF_2-16h in MOPS buffers, respectively. (C) The fluorescence spectra at different times of reaction with 20 μL CDCs-NH_4HF_2-16h added. (D) The fluorescence intensity changes with the addition of different volumes of CDCs-NH_4HF_2-16h of 10, 15, 20, 40, 60, 80, 100, 150 μL. (E) The O_2 emission catalyzed by CDCs-NH_4HF_2-16h at different volumes range from 1 mL–8 mL (1 mL as a unit) in solution of 10 mL 50 mmol/L NaAc (pH = 5).

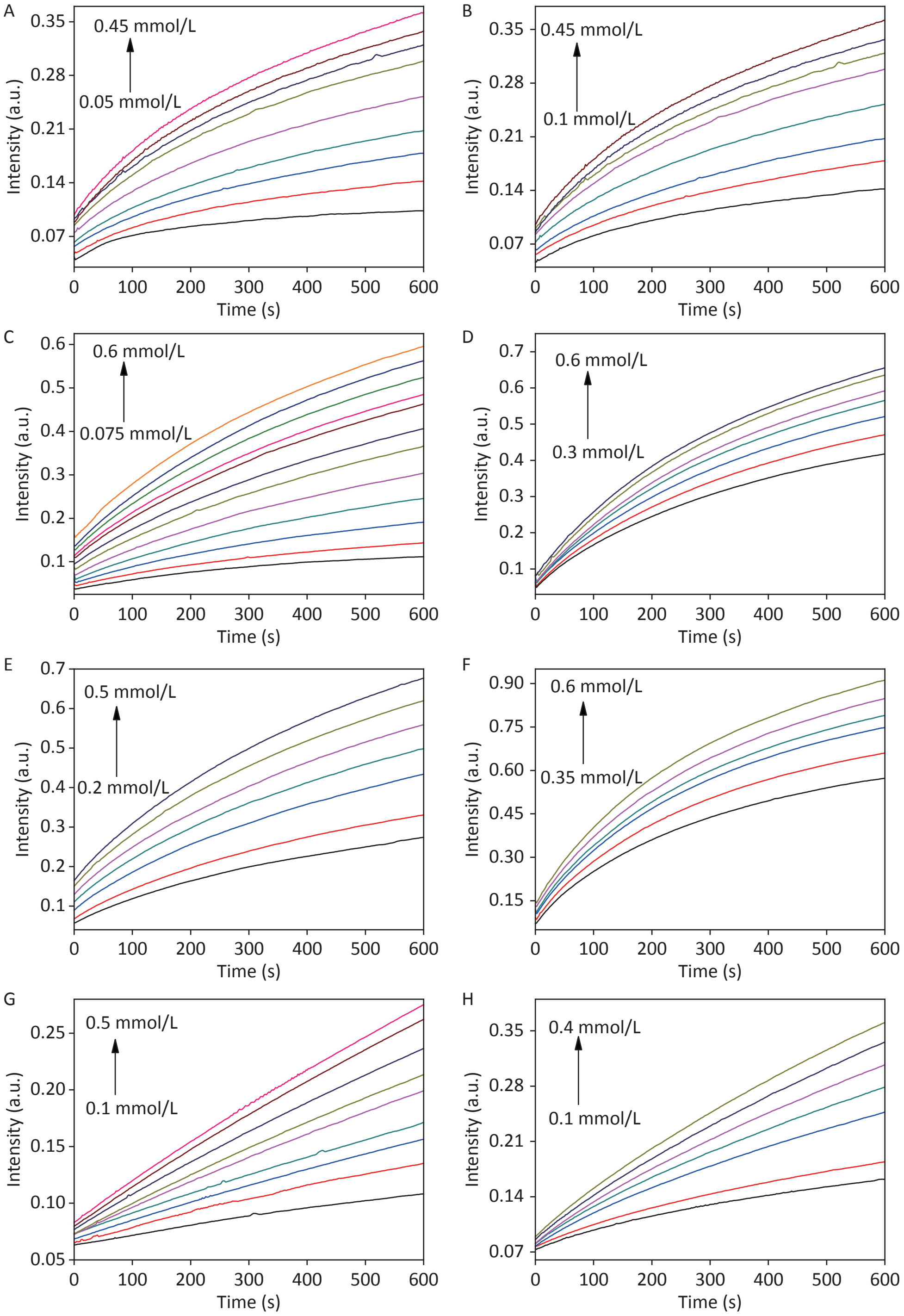

Supplementary Figure S10. Time-dependent absorbance changes of $TMB^{\bullet+}$, generated upon the oxidation of TMB with variable concentrations of TMB (A, C, E, and G) and H_2O_2 (B, D, F, and H) of CDCs-NH_4HF_2-6h, CDCs-NH_4HF_2-12h, CDCs-NH_4HF_2-16h, and CDCs-NH_4HF_2-20h, respectively.

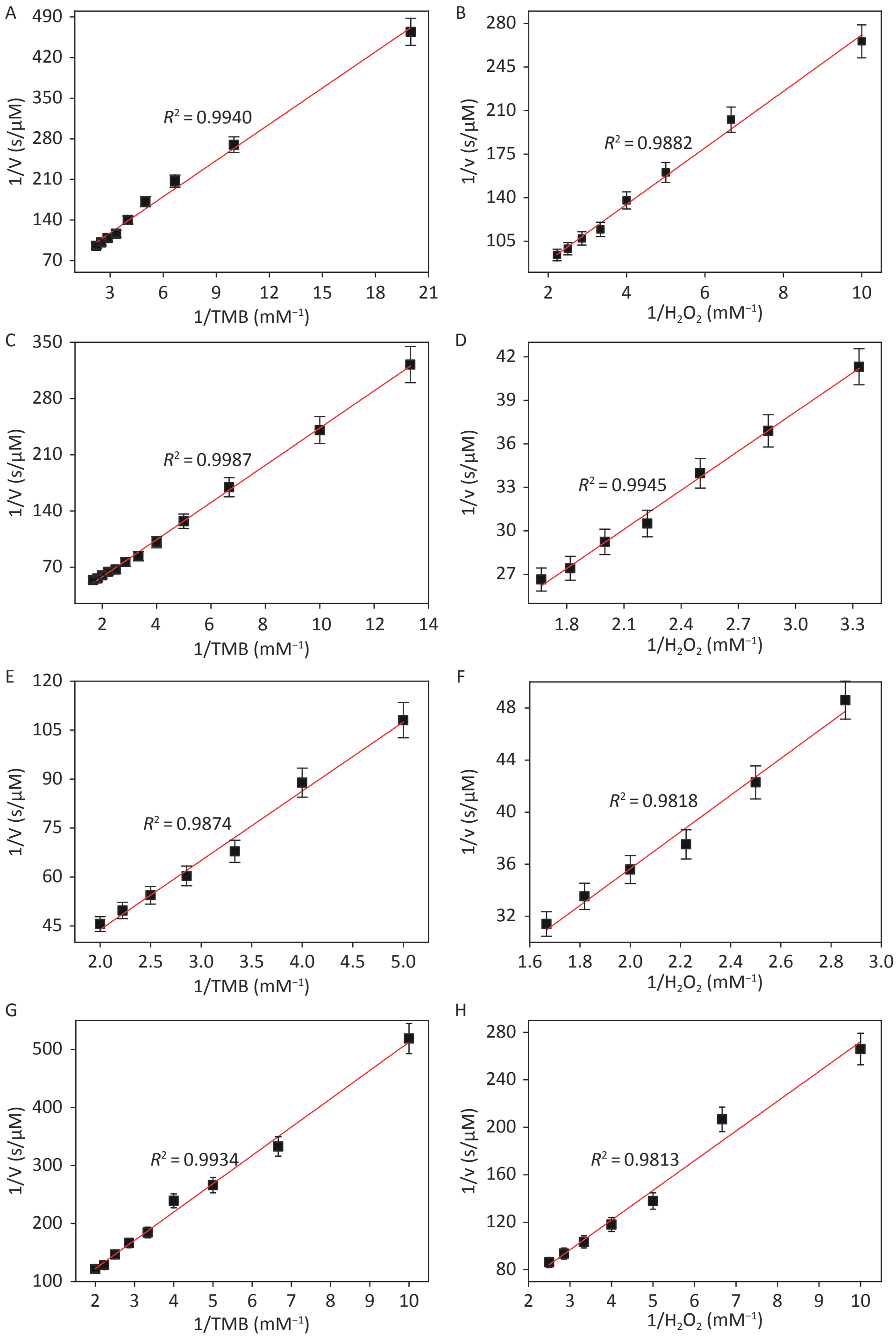

Supplementary Figure S11. Steady-state kinetic assay and catalytic mechanism of CDCs-NH_4HF_2-6h, CDCs-NH_4HF_2-12h, CDCs-NH_4HF_2-16h and CDCs-NH_4HF_2-20h. The double reciprocal plots of activity of CDCs-NH_4HF_2-6h, CDCs-NH_4HF_2-12h, CDCs-NH_4HF_2-16h and CDCs-NH_4HF_2-20h with the concentration of one substrate (H_2O_2 or TMB) fixed and the other varied. The error bars represent the standard deviation for three measurements.

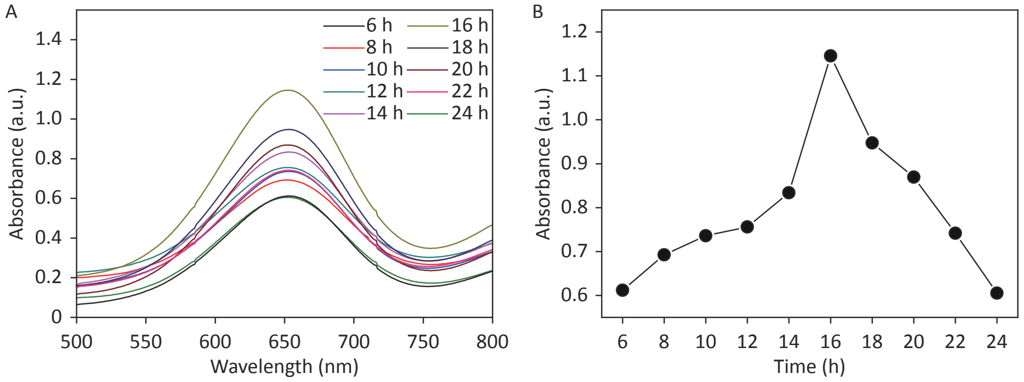

Supplementary Figure S12. The UV absorption spectra of different electrolysis time from 6–24 h (2 h as a unit) after adding TMB (1 mmol/L) and H_2O_2 (50 mmol/L) for 30 min.

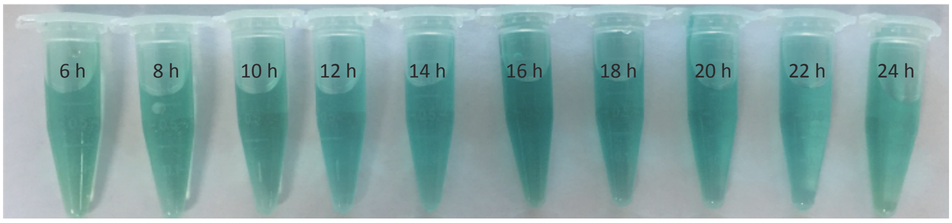

Supplementary Figure S13. The photograph of nanosheets with different electrolysis time from 6–24 h (2 h as a unit) after adding TMB (1 mmol/L) and H_2O_2 (50 mmol/L) for 30 min.

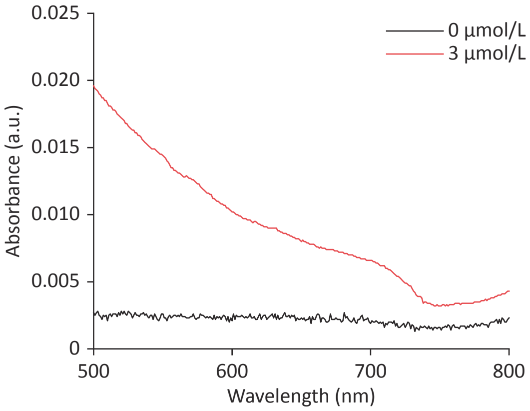

Supplementary Figure S14. UV-vis spectra of CDCs-NH_4HF_2-16h+TMB in the absence (the black line) and presence of 3 μmol/L cholesterol (the red line).

Supplementary Table S1. XPS peak fitting results for CDCs-NH_4HF_2-6h, CDCs-$NaHF_2$-6h, and CDCs-NH_4F-6h

	CDCs-NH_4HF_2-6h	**CDCs-$NaHF_2$-6h**	**CDCs-NH_4F-6h**	
Region	BE [eV]	BE [eV]	BE [eV]	Assigned to
Ti 2p	466	466		TiO_2
	464.9	464.9	465	C-Ti-F_x
	462.9	462.9	462.3	Ti^{3+}
	460.3	460.3	460.3	TiO_2
	459.3	459.3	458.6	C-Ti-F_x
			456.8	Ti^{3+}
O 1s	532.6	533.3	532.8	H_2O
	531.8	532.5	532	C-Ti-$(OH)_x$
	531	531.8	531.3	C-Ti-O_x
	530	531.1	530.5	TiO_2

Supplementary Table S2. XPS peak fitting results for CDCs-NH_4HF_2-6h, CDCs-NH_4HF_2-10h, CDCs-NH_4HF_2-16h, and CDCs-NH_4HF_2-20h

	CDCs-NH_4HF_2-6h	**CDCs-NH_4HF_2-10h**	**CDCs-NH_4HF_2-16h**	**CDCs-NH_4HF_2-20h**	
Region	BE [eV]	BE [eV]	BE [eV]	BE [eV]	Assigned to
C 1s	281.75	282			Ti-C
	284.40	284.55	284.41	284.30	C-C
	284.85	285	285	284.99	C-O
Ti 2p	466	466	465.79	465.80	TiO_2
	464.90	465			C-Ti-F_x
	462.90				Ti^{3+}
	460.25	460.30	460.15	460.03	TiO_2
	459.15	459.40			C-Ti-F_x
O 1s	532.60	532.80	532.13	532.10	H_2O
	531.78	532.10			C-Ti-$(OH)_x$
	531	531.60			C-Ti-O_x
	530.03	530.90	530.50	531	TiO_2

Supplementary Table S3. Comparison of the apparent Michaelis-Menten constant (K_m) and maximum reaction rate (V_{max}) between of CDCs and HRP

Sample	**Substrate**	**Substrate fixed (mmol/L)**	**V_{max} (mM·s^{-1})**	**K_m (mmol/L)**
CDCs-NH_4HF_2-6h	TMB	H_2O_2 (50)	1.80×10^{-5}	0.35
CDCs-NH_4HF_2-6h	H_2O_2	TMB (1)	2.30×10^{-5}	0.52
CDCs-NH_4HF_2-10h	TMB	H_2O_2 (50)	8.50×10^{-5}	1.98
CDCs-NH_4HF_2-10h	H_2O_2	TMB (1)	6.00×10^{-5}	0.86
CDCs-NH_4HF_2-16h	TMB	H_2O_2 (50)	6.80×10^{-4}	14.52
CDCs-NH_4HF_2-16h	H_2O_2	TMB (1)	1.35×10^{-4}	1.90
CDCs-NH_4HF_2-20h	TMB	H_2O_2 (50)	4.00×10^{-5}	1.96
CDCs-NH_4HF_2-20h	H_2O_2	TMB (1)	4.60×10^{-5}	1.20